Available online at www.CivileJournal.org

Civil Engineering Journal

(E-ISSN: 2476-3055; ISSN: 2676-6957)

Vol. 11, No. 06, June, 2025

Structural and Soil Deformations in Non-Invert and Circular Tunnels: A Centrifuge and Numerical Analysis

Abdulaleem Dawood [1*], Katsutoshi Ueno [1]

[1] *Social Infrastructure Systems Program, Graduate School of Science and Technology for Innovation, Tokushima University, Tokushima, 770-8506, Japan.*

Received 22 February 2025; Revised 17 May 2025; Accepted 23 May 2025; Published 01 June 2025

Abstract

Non-invert tunnels are often chosen to reduce initial construction costs compared to circular tunnels, but they frequently require expensive maintenance. Despite their widespread use, limited research has quantified the differences in material requirements (steel and concrete) between these two designs. This study compares the internal forces and material demands of circular and non-invert tunnels using centrifuge model tests and numerical analysis. A combined approach using 40g centrifuge testing and parametric analysis in OPTUM G2 assesses bending moments, lining shear forces, and shear stress distributions. Three tunnel diameters (9 m, 12 m, and 16 m) are analyzed across depth ratios (H/D = 10, 7, 5, and 1), covering eight reinforced concrete lining designs. Results show that circular tunnels have more uniform stress distributions in the lining and surrounding soil, leading to lower bending moments and shear forces. In contrast, non-invert tunnels exhibit stress concentrations near the lower fulcrum corners and spring line. Due to their uniform stress distribution, circular tunnels become more material-efficient than non-invert at greater depths and larger diameters, reducing steel use by up to 36% despite requiring up to 19% more concrete. Non-invert tunnels, however, use less material at shallow depths, saving up to 14% in steel and 23% in concrete.

Keywords: Centrifuge Model Tests; Numerical Analysis; Circular Tunnel Section; Non-Invert Section.

1. Introduction

Tunnel design decisions often prioritize short-term economics, contributing to the widespread use of non-invert geometries (tunnels constructed without reinforced concrete inverts), despite documented evidence of their higher maintenance costs. While circular tunnels are widely recognized for their structural efficiency, non-invert designs remain common in initial construction due to perceived savings in excavation and lining materials. However, the difference in internal forces between these tunnel types, particularly in terms of bending moments and shear forces in the lining, and their direct impact on steel and concrete quantities have not been systematically investigated. To address this gap, this study conducts a parametric analysis using centrifuge and numerical modelling to quantify how variations in the depth-to-diameter (H/D) ratio affect structural behavior and material demand in both tunnel configurations.

Previous studies have demonstrated that non-invert tunnels are prone to deformation under environmental stresses, including swelling, squeezing ground conditions, and water-induced pressure. These deformations frequently necessitate repair measures such as rock bolting, invert installation, or even new tunnel construction leading to elevated maintenance costs and operational disruptions. A notable example is the Tenjin Yama Tunnel, where initial rock bolts failed to mitigate swelling, ultimately requiring the installation of a concrete invert. To prevent traffic interruption affecting 30,000 vehicles per day, a parallel tunnel had to be constructed first [1]. Research demonstrates that installing inverts

* Corresponding author: aleemdawood.jp@gmail.com

http://dx.doi.org/10.28991/CEJ-2025-011-06-02

plays a critical role in stabilizing non-invert tunnels by mitigating floor swelling effects [2–7]. Asakura & Kojima [8] further emphasized this necessity, showing that inverts are essential for controlling heave in squeezing ground conditions. Expanding on these findings, Huang et al. [9] recommended specific design measures proposing invert arch depths of 60 cm for moderate deformation zones and 110 cm for severe zones. Inverts also contribute to enhanced seismic resilience and reduced deformation to emphasizing their essential function in achieving tunnel durability [10–12]. Ground rock bolts play an important role in the non-invert tunnel stability in resisting hydrostatic uplift, presented in the Burnley Tunnel case, which required 5,200 anchors to maintain stability against upward water pressure [13]. Besides, it was used in the weak fracture zone of the Dongmachang Tunnel No. 1 [14].

In contrast, circular tunnels exhibit superior performance due to uniform stress distribution, dynamic load resistance, and hydraulic stability. Saraswat & Maheshwari [15] concluded that circular tunnels have the highest structural resilience under both static and seismic loads owing to their symmetrical shape which avoids stress concentrations that commonly occur in horseshoe or D-shaped tunnels. Ng et al. [16] illustrated that circular tunnels develop 70% lower bending strain (38 $\mu\varepsilon$ vs. 130 $\mu\varepsilon$) and reduced excavation-induced deformation versus horseshoe shapes, due to efficient hoop stress distribution.

Further studies underscore the benefits of circular geometry in complex geological conditions. Ma et al. [17] emphasized the necessity of adopting a circular tunnel cross section in weak interlayered rock strata particularly in contrast to non-invert geometries which exhibited greater instability. Dang et al. [18] confirmed the structural reliability of circular tunnels across a range of rock mass classifications, noting minimal radial displacement compared to alternative shapes. Lopez Ochoa [19], using finite element analysis, found that tunnels without an invert arch exhibited nearly twice the displacement and significantly higher bending moments compared to tunnels with a continuous lining. In terms of hydraulic behavior, Farhadian & Gholami [20] found that circular tunnels consistently exhibited the lowest groundwater inflow and the widest influence radius, outperforming horseshoe, D-shaped, rectangular, and irregular hexagon tunnels. Han et al. [21] found that circular tunnels demonstrate superior stress distribution that reduces strength loss by approximately 23–50% compared to square or elliptical shapes while minimizing crack formation and efficiently transferring loads under both dynamic and static conditions. Nie et al. [22] also noted that circular and elliptical tunnels exhibit superior dynamic stability characterized by minimal stress concentrations and controlled crack propagation. On the other hand, rectangular tunnels performed worse due to shear failures at the corners.

Taken together, prior research yields two key insights:

- Non-invert tunnels are more vulnerable to ground deformation, floor heave, hydrostatic pressure, and dynamic loading, all of which elevate maintenance costs, as exemplified by the Tenjin Yama Tunnel, which required the installation of a new tunnel [1].
- Full circular tunnel sections offer superior structural performance through more uniform stress distribution, reduced internal forces, and enhanced stability under static-, dynamic-, and hydraulic-loading conditions.

Despite the demonstrated advantages of circular tunnels, non-invert designs remain prevalent in practice due to perceived cost savings. However, their open-bottom geometry generates stress concentrations that produce higher bending moments and internal forces than circular designs [15, 19], typically requiring thicker linings and increased steel reinforcement. In contrast, circular tunnels provide greater durability efficiency yet requiring larger cross. A critical gap remains uninvestigated in systematic comparisons of these tunnel types regarding both structural performance and material requirements (concrete and steel quantities).

To address this gap, this study combines centrifuge model testing, numerical simulation, and parametric analysis. Two scaled tunnel models, a full circular section and a non-invert section, are tested under identical conditions in a geotechnical centrifuge. Strain gauges were placed at the crown, shoulder, and springline to measure internal forces and deformation. This approach has been widely applied in prior studies investigating tunnel–soil interaction employing centrifuge modelling [23–25]. The physical modelling results are validated and extended through finite element analysis using OPTUM G2, allowing exploration of soil–structure interaction beyond experimental limitations. A subsequent parametric study examined the influence of varying H/D ratios on lining forces and cost efficiency, comparing material demands to identify conditions under which circular designs offer economic advantages. The research workflow is illustrated in Figure 1.

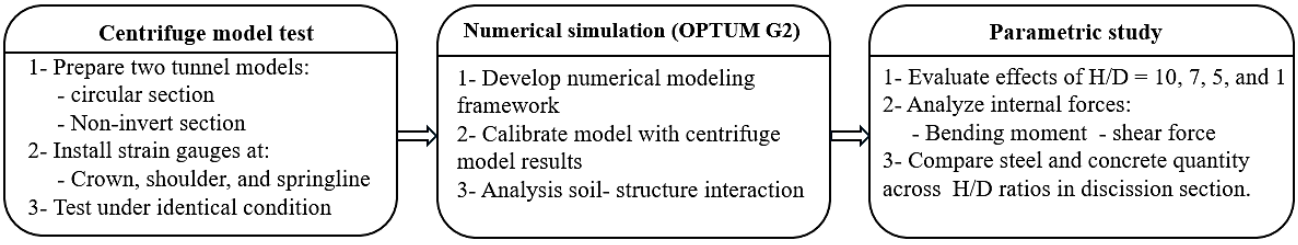

Figure 1. Study Workflow: Experimental, Numerical, and Parametric Tunnel Analysis

The remainder of this paper is organized as follows. Section 2 describes the centrifuge modelling methodology and experimental setup used to compare circular and non-invert tunnel sections. Numerical analysis in Section 3 covers the modelling framework validation procedures and key findings on soil-structure interaction. A parametric study in Section 4 evaluates geometry and depth effects on tunnel performance. Section 5 presents the main structural behavior findings and quantifies steel and concrete requirements. Sections 6 and 7 present the conclusions and study limitations.

2. Centrifuge Model Test

Centrifuge model testing was used to replicate full-scale tunnel behavior under controlled laboratory conditions by applying the principle of similitude. Increased gravitational acceleration (40g) was used to ensure identical stress states between the scaled model (1:N) and the prototype. This approach preserves key dimensionless relationships, as summarized in Table 1, enabling accurate simulation of soil–structure interaction mechanisms. Strain gauges were positioned at critical tunnel sections including the crown, shoulder, and springline to measure internal forces and capture detailed data on stress redistribution.

Table 1. Centrifuge model scale factors

Physical Parameters	Model/Prototype
Length	1/40
Acceleration	40
Stress	1
Strain	1
Force	$1/40^2$
Moment	$1/40^3$

The experimental setup used a centrifuge apparatus developed at the University of Tokushima as shown in Figure 2 with an effective radius of 1.55 meters. The system is capable of generating up to 100g acceleration and supporting loads up to 40 g·tons. It includes an integrated data acquisition system for real-time monitoring of both structural and soil responses. An aluminium model container measuring 45 cm in length, 20 cm in width, and 35 cm in depth was used to maintain structural integrity under high centrifugal forces.

Figure 2. Centrifuge model testing at Tokushima University

Two centrifuge experiments are conducted to compare the structural response of circular and non-invert tunnel sections. Both tests were performed under identical conditions including uniform soil properties, boundary conditions, and model configurations to ensure a valid basis for comparison.

2.1. Tunnel Lining Materials

The tunnel lining is modeled using Unplasticized Polyvinyl Chloride (UPVC), selected for its flexibility and durability which enhances accuracy and reduces the risk of damage during testing. To simulate a non-invert tunnel, a model was constructed with dimensions of 6 cm in diameter, 4.5 cm in height, 20 cm in length, and 4 mm in thickness. This corresponds to a prototype tunnel with a diameter of 2.4 m, a height of 1.8 m, and a wall thickness of 16 cm, based on a 40g scaling factor. As shown in Figure 3-a, the non-invert tunnel model was supported by two small steel plates positioned at the ends of the lining, each measuring 20 cm in length, 1 cm in width, and 0.5 mm in thickness, corresponding to 40 cm in width and 2 cm in thickness at prototype scale. The circular tunnel section model, shown in Figure 3-c, had a diameter of 6 cm, a length of 20 cm, and a thickness of 4 mm, representing a prototype tunnel with a

diameter of 2.4 m and a wall thickness of 16 cm under the same scaling factor. The material properties of the UPVC tunnel lining and the steel support plates are described in the numerical analysis section.

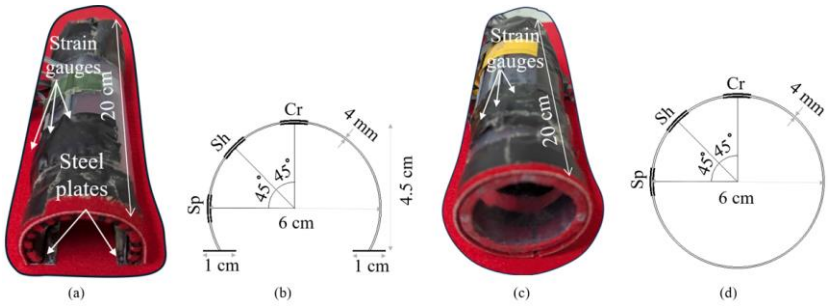

Figure 3. (a) UPVC non-invert tunnel, (b) Strain gauge positions on non-invert tunnel, (c) UPVC circular tunnel, (d) Strain gauge positions on circular tunnel

Six strain gauges are installed on the inner and outer surfaces of the non-invert tunnel at the crown, shoulder, and spring point on the left half of the model. In the circular tunnel section strain gauges are placed at the same locations to enable a direct comparison of strain responses between the two tunnel types. This setup allows for a comprehensive analysis of tunnel–soil interaction and provides insight into the structural behavior of each tunnel type under loading conditions. The strain gauge positions for both models are shown in Figure 3-b and Figure 3-d, where CR, SH, and SP denote the crown, shoulder, and spring point, respectively.

2.2. Model Preparation

Although non-invert tunnels are typically constructed in hard rock formations, modelling rock behavior at small scale presents significant challenges in centrifuge testing. To address this limitation dry silica sand No. 6 was selected as the surrounding soil medium due to its well-documented mechanical properties, ease of handling, and high reproducibility in physical modelling. This approach aligns with Shibayama et al. [26], who employed a non-invert tunnel model embedded in dry sand No. 6 to investigate tunnel behavior under shear deformation in soft soils.

Soil stiffness plays a critical role in influencing load transfer between the surrounding ground and the tunnel lining. In soft soils with a low elastic modulus, such as dry sand, a greater proportion of the structural load is carried by the tunnel lining due to the limited self-support capacity of the surrounding ground. In contrast, stiffer soils facilitate more effective load-sharing through the mechanism of soil arching, thereby reducing the stress imposed on the lining. This phenomenon becomes particularly significant in shallow tunnels, where the reduced overburden height limits the development of soil arching and amplifies the system's sensitivity to variations in soil stiffness [27]. The physical properties of Silica Sand No. 6 and its grain size distribution are shown in Table 2 and Figure 4, respectively.

Table 2. Physical Properties of Silica Sand No. 6

Property	Value
Specific gravity: ρs (g/cm³)	2.644
Maximum void ratio: e_{max}	0.991
Minimum void ratio: e_{min}	0.658
D_{10} (mm)	0.131
D_{30} (mm)	0.185
D_{60} (mm)	0.273

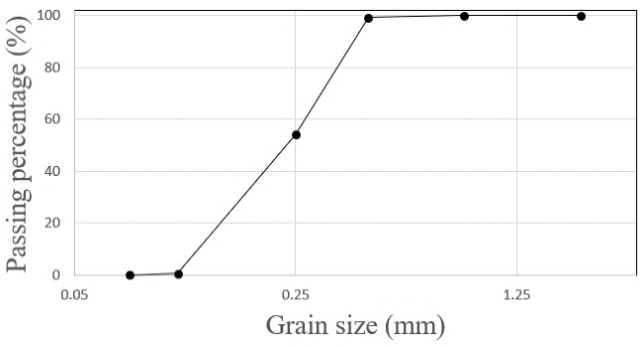

Figure 4. Grain size distribution curve of silica sand No.6

To achieve homogeneous soil conditions, the sand was placed in the container using the air pluviation method which enables controlled and uniform density distribution. The sand was poured from a height of 80 cm, resulting in a relative density of approximately 80%, following the procedure outlined by Ueno [28]. This method minimizes particle segregation and compaction variability, thereby promoting uniform stress conditions during centrifuge loading. The non-invert tunnel model was positioned 17.5 cm from the container base, equivalent to more than three times the tunnel height, while the circular tunnel model was placed at a depth of 16 cm, corresponding to 2.67 times its diameter. Both models were installed with at least three tunnel diameters of clearance from the left and right container boundaries, and one diameter from the top. The dimensions of both models are shown in Figures 5-a and 5-b.

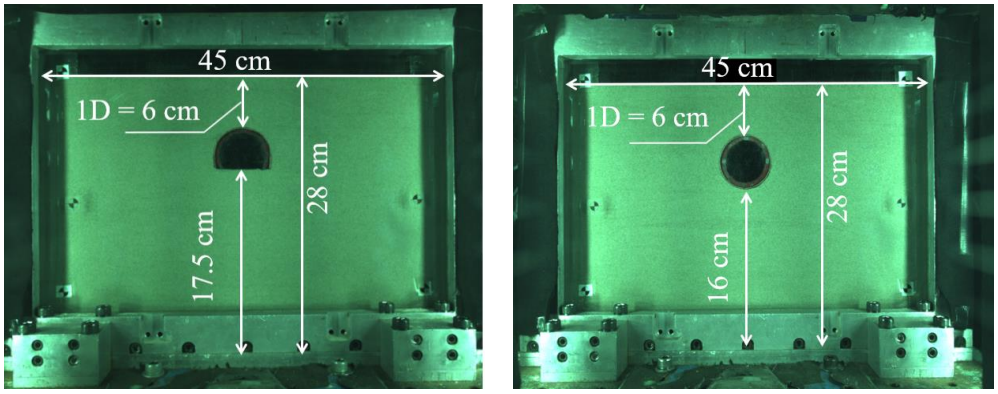

(a) Non-invert model dimension (b) Circular model dimension

Figure 5. Non-invert and circular tunnel models dimensions

2.3. Gauges Measurements and Validation

To evaluate the structural response of the tunnel lining under centrifuge loading, strain gauges are installed at key locations along the tunnel profile, including the crown (Cr), shoulder (Sh), and springline (Sp). These gauges record strain variations and provide insights into the strain distribution around the lining. The centrifuge acceleration was incrementally increased from 5g to 10g, 20g, 30g, and finally 40g as illustrated in Figures 6-a and 6-b. The measured strain values show a progressive increase with rising acceleration, peaking at 40g. At this acceleration the final data analysis is conducted. The recorded strain values for both the non-invert and circular tunnel sections at 40g are summarized in Table 3.

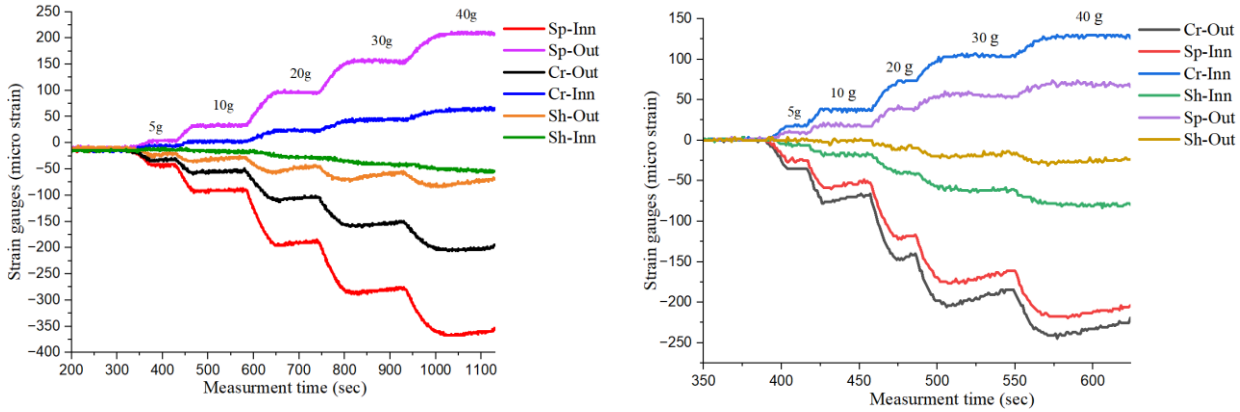

(a) Non-invert tunnel Strain gauge values (b) Circular tunnel Strain gauge values

Figure 6. Non-invert and circular tunnels Strain gauge values

Table 3. Non-invert and circular tunnel Strain gauge values at 40 g

Tunnel	Sp-Out	Sp-Inn	Sh-Out	Sh-Inn	Cr-Out	Cr-Inn
Non-invert tunnel (micro strain)	203.86	-361.13	-83.48	-50.48	-199.98	60.18
Circular tunnel (micro strain)	66.01	-217.54	-27.18	-79.60	-244.64	130.08

The results indicate that the non-invert tunnel experience higher strain concentrations at the springline compared to the crown and shoulder. The peak tensile strain is recorded at the exterior of the spring point (+203.86 με), while peak compressive strain occurs at the interior (-361.13 με), indicating localized bending at the spring point corners, which are known structural weak points in non-invert geometries. The resulting strain differential (Δ564.99 με) highlights a

location where the tunnel lining bends the most. All measured strain values remained well below the yield strain of UPVC, which is approximately 1000 με.

In contrast, the circular tunnel, which includes a continuous lining with an invert, exhibits a more symmetric and balanced strain distribution. Peak tensile strain is observed at the inner crown (+130.08 με) and peak compressive strain at the outer crown (-244.64 με), resulting in a smaller strain differential (Δ374.72 με) compared to non-invert tunnel. The uniform strain pattern indicates that the circular tunnel remained within the elastic range of UPVC and displays stable ring compression behavior, characteristic of well-confined tunnel structures under symmetric loading.

To validate the centrifuge model results, a numerical analysis is conducted by calculating bending moments along the tunnel lining. The moment is determined using Equation 1 derived from strain readings at key locations (crown, shoulder, and springline), and compared with numerical simulation results.

$$M = \frac{(\varepsilon_{outer} - \varepsilon_{inner})}{2} \times \frac{E \times I}{c} \quad (1)$$

In this equation, ε_{outer} and ε_{inner} represent the outer and inner surface strains respectively. E denotes the modulus of elasticity (taken as 3 MPa), I is the moment of inertia, and c is the distance from the neutral axis to the outermost surface. The moment distributions for both tunnels obtained from the centrifuge model (C.M.) are illustrated in Figure 9 (in Section 3.4.) and exhibit a close comparison with the numerical analysis findings.

3. Numerical Analysis

3.1. Model Dimensions

A two-dimensional elastoplastic model employing the Mohr–Coulomb failure criterion is developed using OPTUM G2 software [29]. The analysis is based on a 40g centrifuge scaling system, where the physical model dimensions were 45 cm in width and 28 cm in height. Accordingly, the numerical model is scaled to 18 m in width and 11.2 m in height. Under the same scaling conditions, the tunnel is modelled with a diameter of 2.4 m, a lining thickness of 16 cm, and an overburden depth equal to one tunnel diameter 2.4 m. The steel support plates at the tunnel base are modelled with a width of 0.4 m and a thickness of 2 cm.

3.2. Input Parameters

The UPVC tunnel lining and the steel support plates are modeled using plate elements in OPTUM G2 under plane strain conditions. The tunnel lining is assigned mechanical properties representative of UPVC [30] with a thickness of 16 cm. The steel plates, placed at the tunnel base, are modeled as fixed plate elements with a thickness of 2 cm. Input parameters for both the lining and the steel plates are calculated using standard equations for plate elements and values provided in the OPTUM G2 manual based on Parameter Set B. In this model, b = 100 cm represents the unit width of the plate, and t is the actual thickness of the lining or plate as shown in Figure 7. The geometric properties including sectional area A, weight per unit length w, material density ρ, plastic section modulus s, and moment of inertia I, are determined using the following equations.

$$A = b \cdot t \quad (2)$$

$$w = A \cdot \rho \quad (3)$$

$$S = 1/4.\, b \cdot t^2 \quad (4)$$

$$I = 1/12\,.\, b \cdot t^3 \quad (5)$$

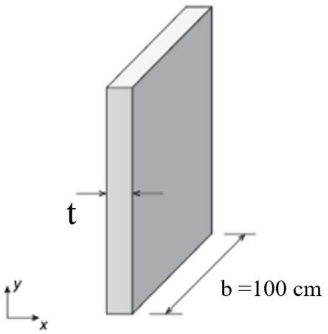

Figure 7. Plate element geometry in OPTUM G2

The calculated values for the UPVC tunnel lining and the steel support plates are summarized in Table 4.

Table 4. UPVC Tunnel lining and Steel Support Properties

Property	UPVC lining	Steel support Plates
Young's Modulus, E (MPa)	3000	200000
Yield Strength, σ0 (MPa)	50	205
Weight, w (kg/m)	224	150
Sectional Area, A (cm²/m)	1600	200
Plastic Section Modulus (cm³/m)	6400	100
Moment of Inertia, I (cm^4 /m)	34133	66.67

Since the experimental relative density is approximately 80%, the soil was classified is medium to dense sand. The Mohr–Coulomb soil properties corresponding to medium sand available in the default material library of OPTUM G2 are used in the numerical analysis. The material properties of dry silica sand No. 6 are summarized in Table 5 and show close agreement the properties reported in Shibayama et al. [26].

Table 5. MC Sand Properties

Property	Value
Unit Weight, γ_{dry} (kN/m³)	16
Poisson's Ratio, ν	0.25
Friction Angle, ϕ °	35
Dilation Angle, ψ °	5
Young's Modulus, E (MPa)	35

3.3. Boundary, Mesh, and Analysis Stages

Standard boundary conditions are applied by assigning roller supports along the vertical boundaries and pinned supports along the horizontal boundaries of the model domain. A refined mesh is generated around the tunnel lining and the steel support plates to improve numerical accuracy. Figures 8-a and 8-b illustrates the mesh and the dimensions of the numerical models.

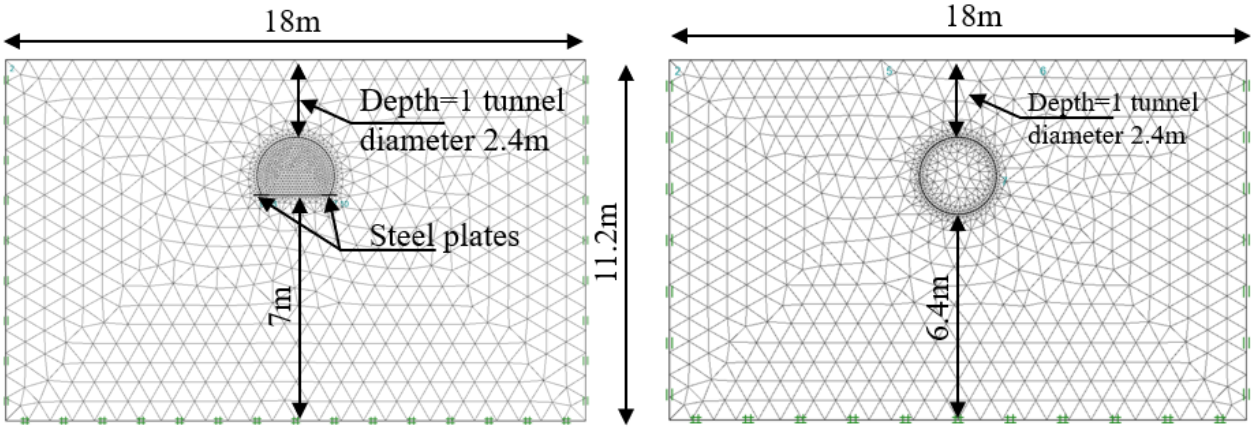

(a) Non-invert tunnel numerical model (b) Circular tunnel numerical model

Figure 8. Non-invert and circular tunnels numerical models' dimensions

The simulation is carried out in three sequential stages to replicate the tunnel construction process and evaluate the development of internal forces within the tunnel lining:

- Stage 1– Initial Setup: The numerical model is configured by defining the geometry and generating the mesh. Material properties are assigned to the soil, tunnel lining, and support plates, followed by setting boundary conditions and computing the initial stress state.

- Stage 2 – Excavation: Tunnel excavation simulated by removing the soil elements within the tunnel zone. Temporary full support applied along the excavation boundary to maintain stability during this phase.
- Stage 3 – Lining Installation: After excavation, the temporary support removed, and the permanent tunnel lining was introduced as a plate element along the tunnel perimeter. The elastoplastic analysis was then carried out to get the result of tunnel lining forces and soil–structure interaction effects.

3.4. Numerical Analysis Results

The numerical analysis compares the structural performance of circular and non-invert tunnel sections, focusing on bending moments, shear forces, and soil shear stress. These two configurations provide valuable insights into the distribution of internal forces and stress concentrations, highlighting key differences in structural behavior. Achieving a uniform distribution of bending moments and shear forces is essential for efficient tunnel lining design. Balanced internal forces enable symmetrical reinforcement layouts, which simplify construction and reduce material costs. This uniformity also minimizes stress concentration, improves crack control, and enhances durability [31-34].

Figures 9-a and 9-b illustrates the bending moment distributions in both tunnel types. In the circular tunnel, positive moments peak at the crown 2.12 kNm/m, while negative moments reach −1.88 kNm/m at the springline. This relatively balanced distribution around the tunnel circumference simplifies the design process by reducing moment variability. In contrast, the non-invert tunnel which lacks structural continuity at the invert exhibits greater moment variation. Positive moments peak at the crown 1.10 kNm/m, while negative moments reach −3.17 kNm/m at the springline. This pattern aligns with the findings of Lopez [19], who reported maximum moment concentrations between the fulcrum corners and spring point in non-invert tunnels, attributing it to the absence of the invert.

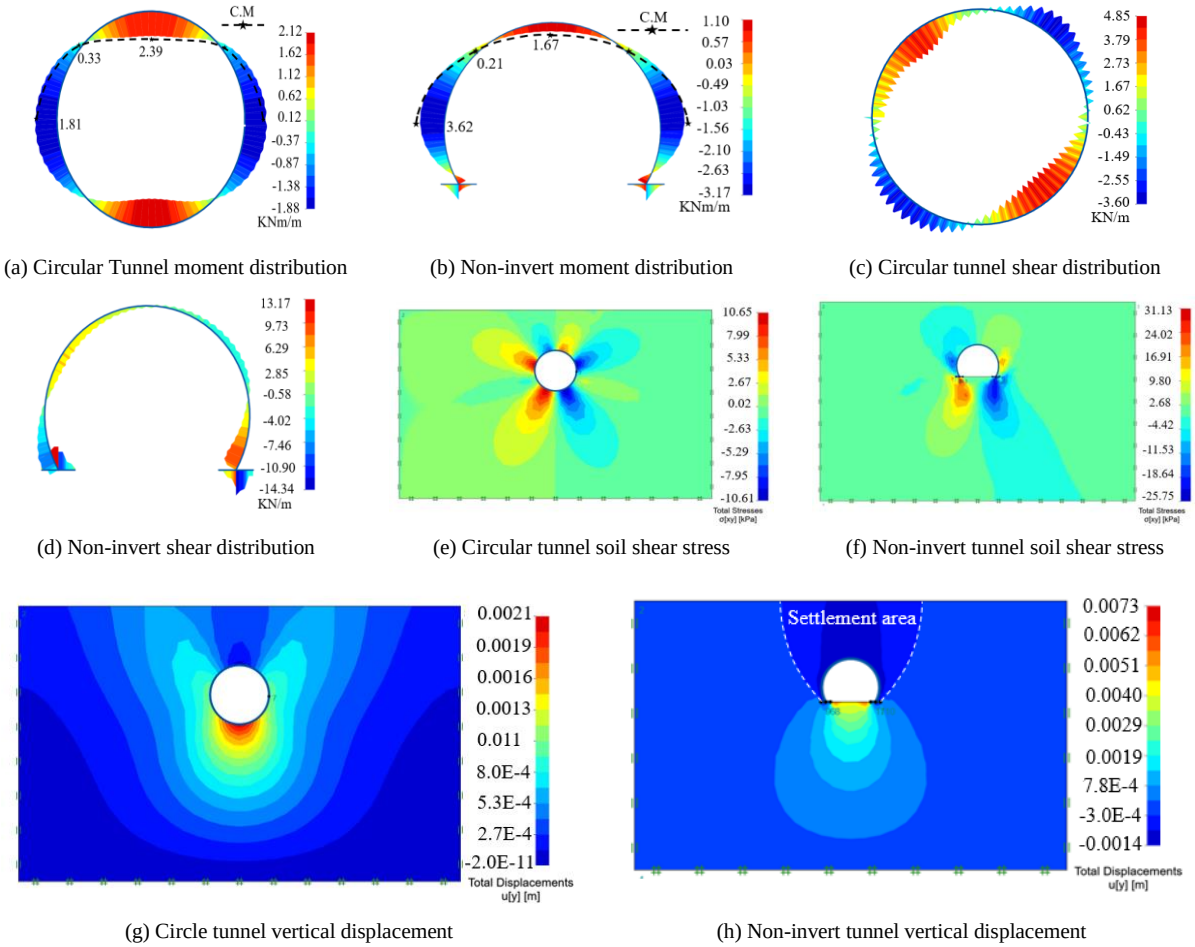

(a) Circular Tunnel moment distribution (b) Non-invert moment distribution (c) Circular tunnel shear distribution

(d) Non-invert shear distribution (e) Circular tunnel soil shear stress (f) Non-invert tunnel soil shear stress

(g) Circle tunnel vertical displacement (h) Non-invert tunnel vertical displacement

Figure 9. Bending moment, shear force, soil shear stress distribution, and vertical displacement for circular and non-invert tunnels

Figures 9-c and 9-d shows the shear force distributions. In the circular tunnel, shear force is distributed relatively uniformly along the lining, with a maximum value of approximately 4.85 kN/m. This symmetrical pattern indicates a

balanced structural response. In contrast, the non-invert tunnel displays concentrated shear forces near the lower fulcrum corners, with a peak of 9.11 kN/m, which is nearly double that of the circular configuration. This underscores the effect of the missing invert on stress concentration.

Figures 9-e and 9-f presents the soil shear stress distributions. In the circular tunnel, shear stress, defined as the component acting on a plane normal to the x-axis in the y-direction, is symmetrically distributed around the circumference with values reaching up to 10.65 kPa. This balanced stress field promotes structural stability and prevents localized deformation. In contrast, the non-invert tunnel exhibits a more uneven stress distribution, with shear stress concentrations near the springline and fulcrum corners, reaching 31.13 kPa, which is nearly three times higher than in the circular tunnel. This finding is consistent with Zeng et al. [35], who noted that stress is highest at corners and sharp transitions in tunnels with irregular shapes, such as D-shaped tunnels.

Figures 9-g and 9-h presents the vertical displacement patterns for both tunnel types. The circular tunnel section exhibits a more stable upper surface, whereas the non-invert section shows noticeable settlement, particularly above the tunnel crown. Although the maximum vertical displacement in the non-invert configuration is relatively small (0.0014 m), it reflects a higher tendency for surface settlement compared to the circular tunnel. Both geometries exhibit soil heave at the invert level. However, the non-invert section experiences 3.5 times greater heave (0.0073 m vs. 0.0021 m). These results highlight the critical role of continuous lining in the circular design for controlling deformation and reveal the inherent susceptibility of open-invert configurations to base heave due to reduced structural continuity.

Overall, the circular tunnel section demonstrates superior structural performance due to its uniform distribution of bending moment, shear force, soil shear stress, and vertical displacement, reducing the need for additional reinforcement. In contrast, the non-invert tunnel requires greater reinforcement to address higher moments and shear concentrations and localized stress, which may lead to increase maintenance demands.

4. Parametric Study

The parametric study used to evaluate the structural performance of tunnels with varying sizes and depths, specifically to determine the conditions under which a full tunnel section is more cost-effective compared to a non-invert section, based on the distribution of moments and shear forces. Due to practical challenges in performing centrifuge model tests for tunnels with varying depths and large diameters, a numerical analysis model is employed which follows the same steps and sequences used in the validated centrifuge model test results. In this study, tunnel diameters of 16 m, 12 m, and 9 m, each with a lining thickness of 30 cm, are considered for both full tunnel sections and non-invert sections. Figures 10-a, 10-b, and 10-c illustrates the full tunnel and the non-invert tunnel sections.

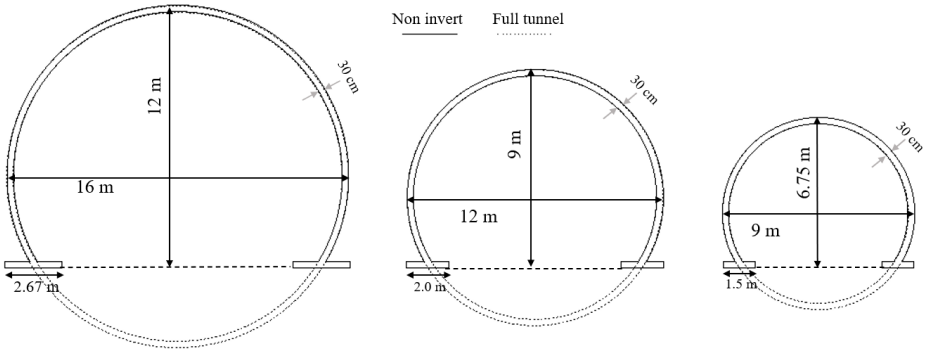

(a) Diameter 16 m (b) Diameter 12 m (c) Diameter 9 m

Figure 10. Circular and Non-Invert Tunnel Sections

The depth of the tunnel is determined using the Depth-to-Diameter Ratio (H/D), calculated from the largest tunnel diameter 16 m, with ratios of (10, 7, 5, and 1) resulting in depths of 160 m, 112 m, 80 m, and 16 m, respectively. To maintain uniformity across simulations, the model dimensions for all cases are set to 240 m × 240 m to provide sufficient space to minimize boundary effects. The tunnel lining properties used in the simulation are shown in Table 6. The simulation incorporates weak rock conditions to replicate challenging ground environments [36-40] and enable a comparative evaluation of the structural behavior of non-invert and circular tunnel sections under difficult conditions. In this study, highly weathered siltstone is used as the representative weak rock material [41]. The rock characteristics are detailed in Table 7.

Table 6. Tunnel lining Properties

Property	Concrete
Young's Modulus, E (MPa)	20000
Yield Strength, σ0 (MPa)	30
Weight, w (kg/m)	750
Sectional Area, A (cm²/m)	3000
Plastic Section Modulus (cm³/m)	22500
Moment of Inertia, I (cm⁴ /m)	225000

Table 7. Highly weathered siltstone Properties [41]

Property	Value
Unit Weight, γdry (kN/m³)	20.8
Poisson's Ratio, ν	0.28
Friction Angle, ϕ °	35
Cohesion, *c* (kPa)	100
Young's Modulus, E (MPa)	100

4.1. Parametric Results at H/D = 10 (Depth = 160 m)

Numerical analysis of full circular tunnels with diameters of 16 m, 12 m, and 9 m at a depth of 160 m yields maximum bending moments of approximately 294 kNm, 307 kNm, and 422 kNm, respectively as shown in Figures 11-a, 11-b, and 11-c. In the non-invert tunnel configuration, the bending moment at the tunnel base remains relatively constant at around 675 kNm, regardless of diameter. Maximum moments along the tunnel lining in this configuration also remain consistent at approximately 675 kNm, particularly near the springline as illustrated in Figures 11-d, 11-e, and 11-f.

A comparison of moment magnitudes between circular and non-invert tunnels of the same diameter indicates that the non-invert configuration consistently exhibits significantly higher values. For the 16 m and 12 m tunnels, the maximum moment in the non-invert configuration is more than twice that of the corresponding circular tunnels. For the 9 m tunnel, the difference remains notable with the non-invert moment approximately 1.5 times greater. These findings highlight the structural inefficiency of non-invert tunnels at greater depths and underscore the advantages of circular tunnel geometry in reducing bending moment.

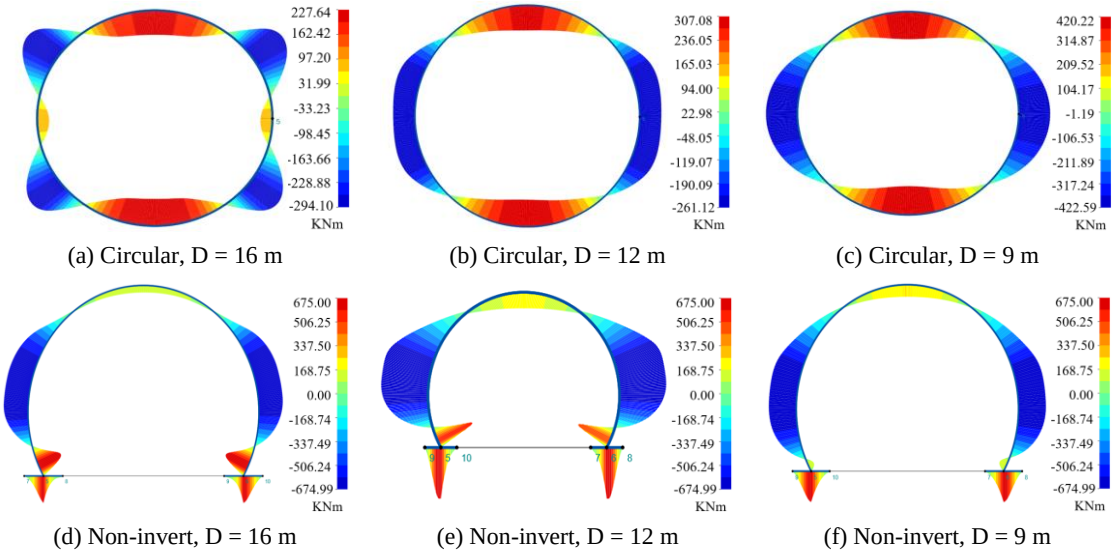

(a) Circular, D = 16 m (b) Circular, D = 12 m (c) Circular, D = 9 m

(d) Non-invert, D = 16 m (e) Non-invert, D = 12 m (f) Non-invert, D = 9 m

Figure 11. Circular and non-invert tunnels bending moment distribution at H/D = 10, (depth = 160m)

At a depth of 160 m, the analysis of shear force distribution indicates that the circular tunnel configuration is associated with significantly lower maximum shear forces compared to the non-invert configuration. For circular tunnels with diameters of 16 m, 12 m, and 9 m, the peak shear forces are 215 kN, 174 kN, and 267 kN, respectively as shown in Figures 12-a, 12-b, and 12-c. In contrast, the non-invert configuration demonstrates substantially higher shear forces: 2022 kN for the 16 m tunnel, 2527 kN for the 12 m tunnel, and 1802 kN for the 9 m tunnel as shown in Figures 12-d, 12-e, and 12-f.

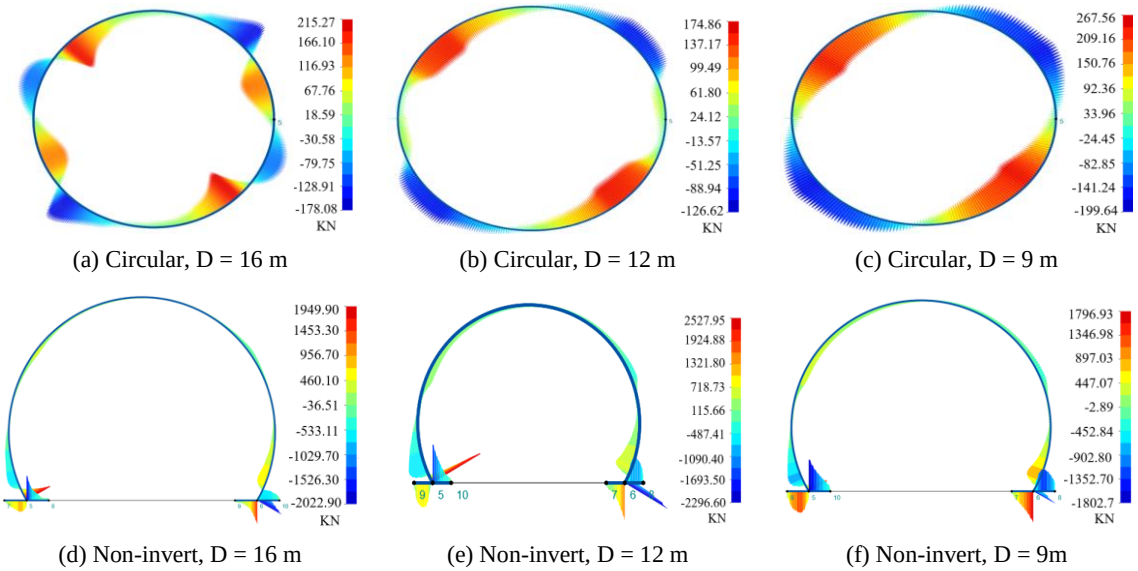

(a) Circular, D = 16 m (b) Circular, D = 12 m (c) Circular, D = 9 m

(d) Non-invert, D = 16 m (e) Non-invert, D = 12 m (f) Non-invert, D = 9m

Figure 12. Circular and non-invert tunnels shear force distribution at H/D = 10, (depth = 160m)

This pronounced disparity highlights the structural efficiency of the circular tunnel geometry in facilitating a more uniform shear force distribution. By comparison, the non-invert configuration exhibits shear force concentrations particularly at the tunnel base and the connection zone between the lining and base. These localized peaks necessitate additional structural reinforcement to ensure stability and maintain safe performance under deep burial conditions.

4.2. Parametric Results at H/D = 7 (Depth = 112 m)

At a depth of 112 m, the maximum bending moments for circular tunnels are approximately 177 kNm for the 16 m tunnel, 244 kNm for the 12 m tunnel, and 339 kNm for the 9 m tunnel as shown in Figures 13-a, 13-b, and 13-c. In the non-invert tunnel configuration at the same depth, the moment distribution remains concentrated near the springline and tunnel base, with maximum values of approximately 675 kNm as illustrated in Figures 13-d, 13-e, and 13-f. For the 16 m and 12 m tunnels, bending moments in the non-invert configuration are more than twice those of the corresponding circular tunnels. In the case of the 9 m tunnel, the non-invert moment is approximately two times greater than that of the circular configuration

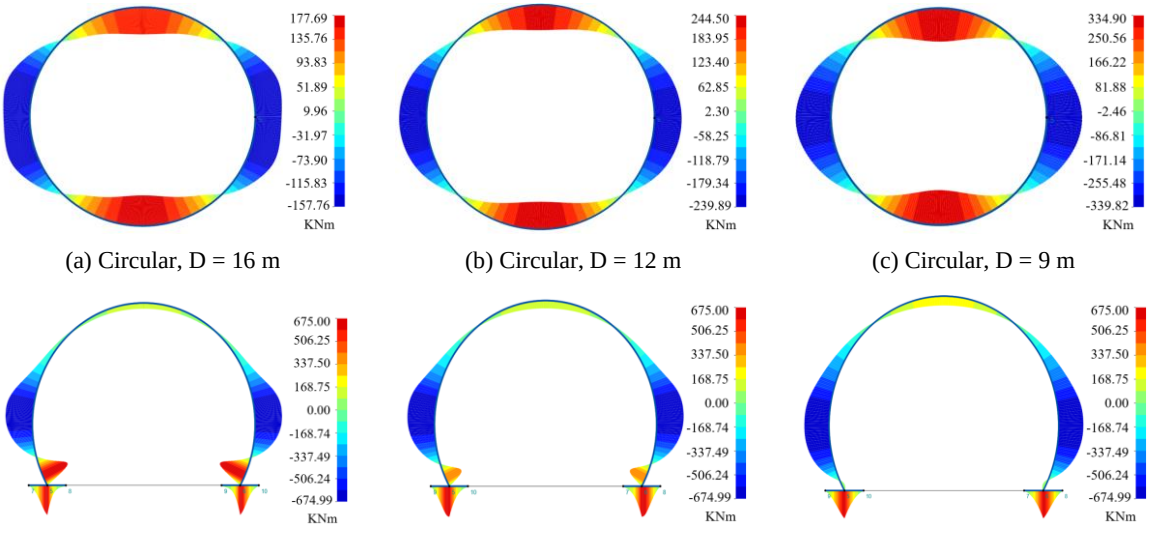

(a) Circular, D = 16 m (b) Circular, D = 12 m (c) Circular, D = 9 m

(d) Non-invert, D = 16 m (e) Non-invert, D = 12 m (f) Non-invert, D = 9 m

Figure 13. Circular and non-invert tunnels bending moment distribution at H/D = 7, (depth = 112 m)

The analysis of shear force distribution at a depth of 112 m indicates that the circular tunnel configuration continues to exhibit relatively small maximum shear values compared to the non-invert configuration. Specifically, the maximum shear forces in the circular tunnel section for diameters of 16 m, 12 m, and 9 m are 96 kN, 141 kN, and 201 kN, respectively as shown in Figures 14-a, 14-b, and 14-c. In contrast, the non-invert tunnel exhibits significantly higher

maximum shear forces of 2013 kN, 2091 kN, and 1755 kN for the same diameters, respectively as shown in Figures 14-d, 14-e, and 14-f. This consistent difference highlights that the circular tunnel configuration maintains a well-distributed shear force pattern with lower values, while the non-invert configuration shows significantly elevated shear forces particularly at the base and at the connection zone between the tunnel lining and the base.

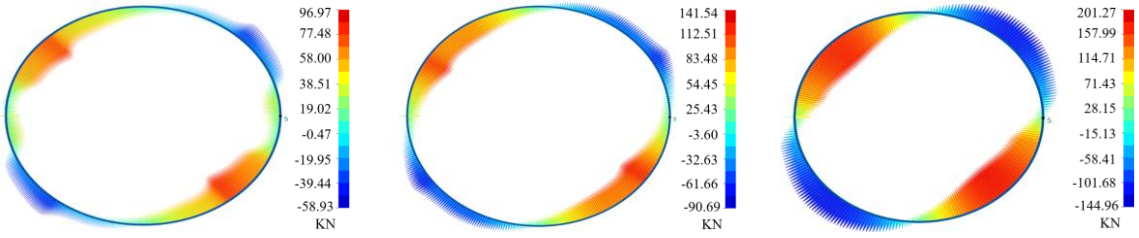

(a) Circular, D = 16 m (b) Circular, D = 12 m (c) Circular, D = 9 m

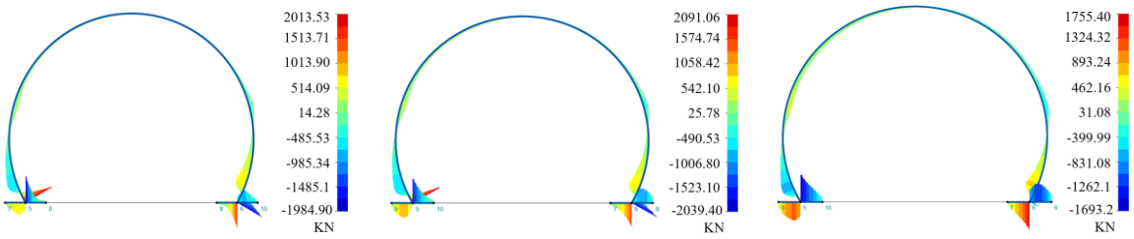

(d) Non-invert, D = 16 m (e) Non-invert, D = 12 m (f) Non-invert, D = 9 m

Figure 14. Circular and non-invert tunnels shear force distribution at H/D = 7, (depth = 112m)

4.3. Parametric Results at H/D = 5 (Depth = 80 m)

The numerical analysis of circular tunnels with diameters of 16 m, 12 m, and 9 m at a depth of 80 m yields maximum bending moments of approximately 144 kNm for the 16 m tunnel, 198 kNm for the 12 m tunnel, and 250 kNm for the 9 m tunnel as shown in Figures 15-a, 15-b, and 15-c. In the non-invert tunnel configuration at the same depth, the moment distribution at the tunnel base remains nearly constant at approximately 675 kNm across all diameters which is consistent with the pattern observed at greater depths as shown in Figures 15-d, 15-e, and 15-f. However, a reduction in maximum bending moments along the tunnel lining (springline) is observed at this depth with values of 537 kNm for the 12 m tunnel and 533 kNm for the 9 m tunnel. This contrasts with the lining moment values of 675 kNm recorded at depths of 160 m and 112 m.

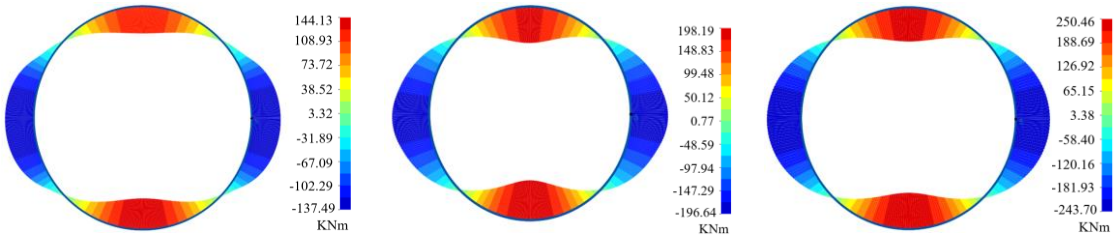

(a) Circular, D = 16 m (b) Circular, D = 12 m (c) Circular, D = 9 m

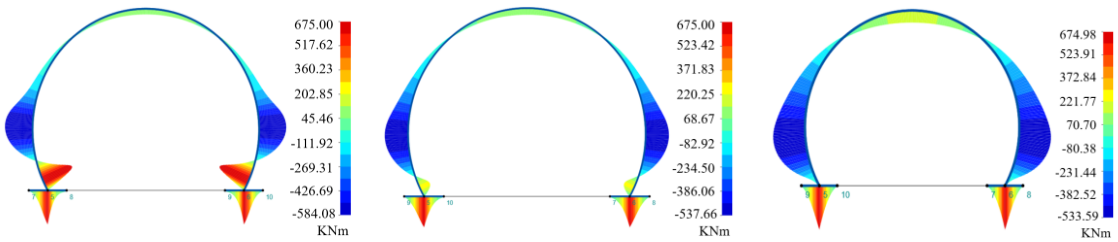

(d) Non-invert, D = 16 m (e) Non-invert, D = 12 m (f) Non-invert, D = 9m

Figure 15. Circular and non-invert tunnels bending moment distribution at H/D = 5, (depth = 80m)

The analysis of shear force distribution at a depth of 80 m indicates that the circular tunnel configuration continues to exhibit relatively low maximum shear forces compared to the non-invert configuration. Specifically, the maximum shear forces in the circular tunnel section for diameters of 16 m, 12 m, and 9 m are 83 kN, 106 kN, and 153 kN, respectively as shown in Figures 16-a, 16-b, and 16-c. In contrast, the non-invert tunnel exhibits significantly higher maximum shear forces of 1972 kN, 1652 kN, and 1703 kN for the same diameters, respectively as shown in Figures 16-

d, 16-e, and 16-f. This consistent difference demonstrates that the circular tunnel configuration achieves a more uniform shear force distribution with lower values, while the non-invert configuration produces elevated shear forces particularly at the base and at the connection zone between the tunnel lining and the base.

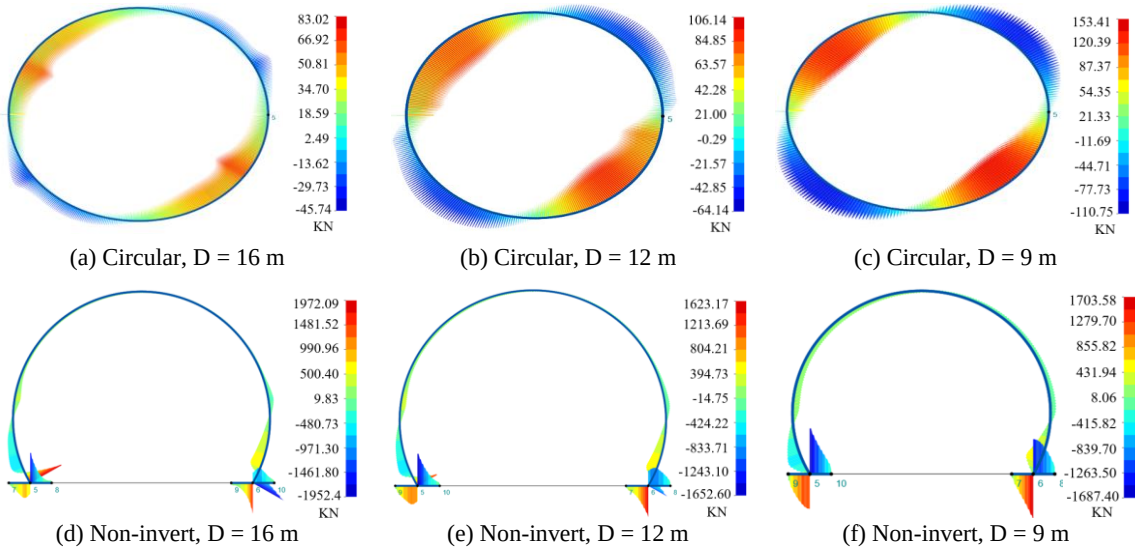

(a) Circular, D = 16 m (b) Circular, D = 12 m (c) Circular, D = 9 m

(d) Non-invert, D = 16 m (e) Non-invert, D = 12 m (f) Non-invert, D = 9 m

Figure 16. Circular and non-invert tunnels shear force distribution at H/D = 5, (depth = 80m)

4.4. Parametric Results at H/D = 1 (Depth = 16 m)

The numerical analysis of circular tunnels with diameters of 16 m, 12 m, and 9 m at a depth of 16 m yields maximum bending moments of approximately 47 kNm, 55 kNm, and 65 kNm, respectively as shown in Figures 17-a, 17-b, and 17-c. In the non-invert tunnel configuration at the same depth, the moment distribution at the tunnel base is approximately 675 kNm for the 16 m tunnel, 422 kNm for the 12 m tunnel, and 252 kNm for the 9 m tunnel as shown in Figures 17-d, 17-e, and 17-f. Additionally, the maximum bending moments along the tunnel lining are 188 kNm for the 16 m tunnel, 95 kNm for the 12 m tunnel, and 66 kNm for the 9 m tunnel. These values represent a noticeable decrease in lining moment magnitudes compared to those recorded at greater depths.

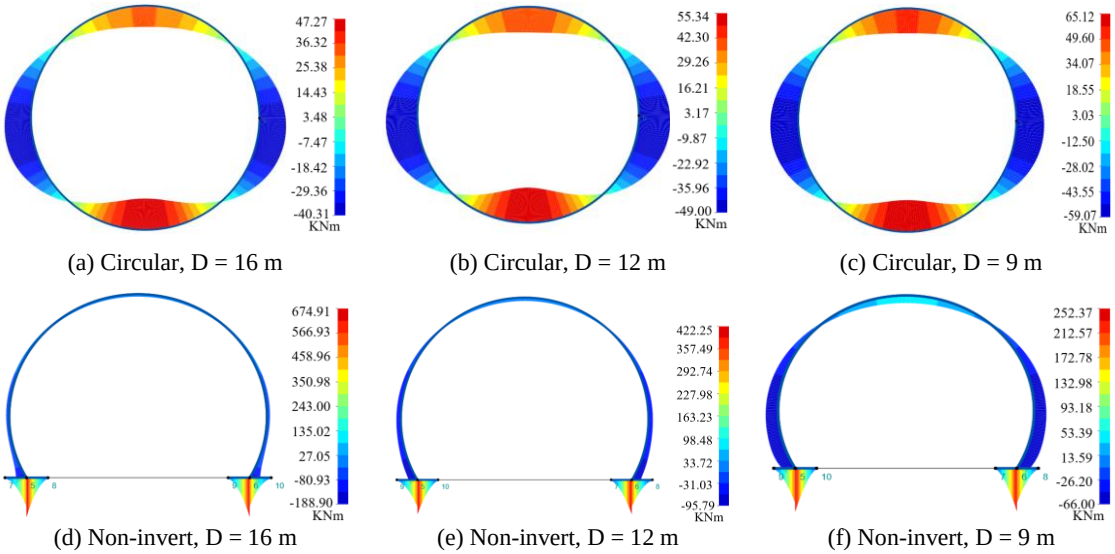

(a) Circular, D = 16 m (b) Circular, D = 12 m (c) Circular, D = 9 m

(d) Non-invert, D = 16 m (e) Non-invert, D = 12 m (f) Non-invert, D = 9 m

Figure 17. Circular and non-invert tunnels bending moment distribution at H/D =1, (depth = 16m)

The analysis of shear force distribution at a depth of 16 m indicates that the circular tunnel configuration continues to exhibit relatively low maximum shear forces compared to the non-invert configuration. Specifically, the maximum shear forces in the circular tunnel section for diameters of 16 m, 12 m, and 9 m are 23 kN, 29 kN, and 39 kN, respectively as shown in Figures 18-a, 18-b, and 18-c. In contrast, the non-invert configuration exhibits significantly higher maximum shear forces of 944 kN, 710 kN, and 535 kN for the same diameters, respectively as shown in Figures 18-d, 18-e, and 18-f. This consistent difference demonstrates that the circular tunnel configuration achieves a more uniform shear force distribution with lower values, while the non-invert configuration results in considerably elevated shear forces particularly at the base.

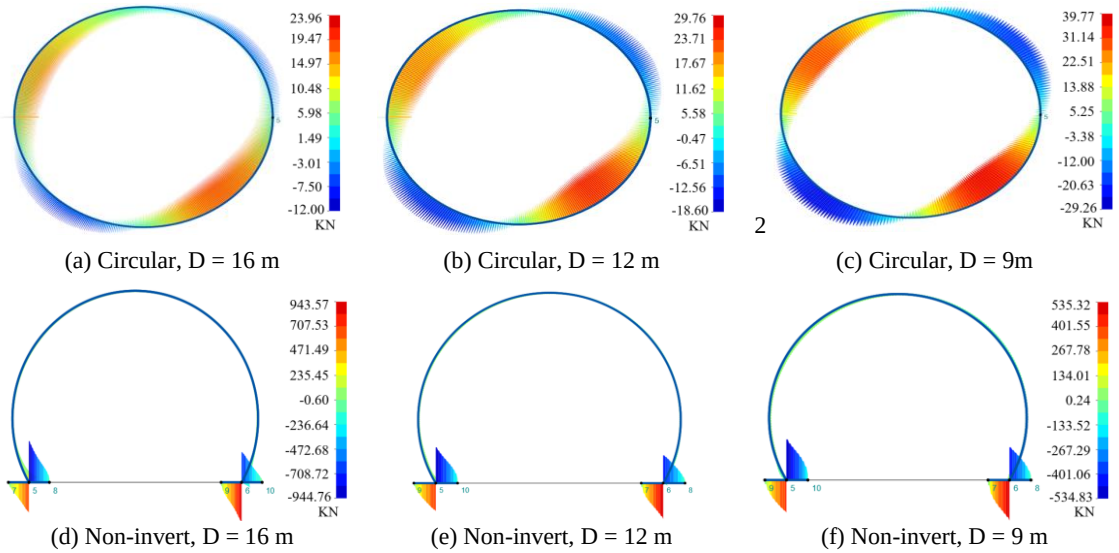

(a) Circular, D = 16 m (b) Circular, D = 12 m (c) Circular, D = 9m

(d) Non-invert, D = 16 m (e) Non-invert, D = 12 m (f) Non-invert, D = 9 m

Figure 18. Circular and non-invert tunnels shear force distribution at H/D = 1, (depth = 16m)

5. Discussion

5.1. Findings from Parametric Study

- Influence of Depth-to-Diameter Ratio (H/D):

  The depth-to-diameter ratio significantly affects the magnitude of internal forces. At H/D = 10 (depth = 160 m) both bending moments and shear forces reach their highest value. As the depth decreases, these forces are progressively reduced. At H/D = 1 (depth = 16 m) the bending moments and shear forces in both tunnel configurations are substantially lower, reflecting the reduced structural demand under shallow burial conditions.

- Effect of Tunnel Cross-Sectional Shape:

  Tunnel geometry plays a critical role in structural performance. Circular tunnels promote more uniform stress distribution leading to lower peak bending moments and shear forces. In contrast, non-invert configurations exhibit localized force concentrations, especially lower fulcrum corners and springline. These stress intensities become more pronounced as burial depth increase highlighting the geometric disadvantages of non-invert sections under high overburden pressure.

5.2. Cost Estimation

To assess the required quantities of concrete and steel reinforcement, eight tunnel lining designs are developed. These sections varied in thickness from 300 mm to 400 mm and include different steel reinforcement layouts. For each design the maximum moment M_n and maximum shear force V_n are calculated using the following equations [42]:

$$M_n = A_s \cdot f_y \cdot d \quad (6)$$

$$V_n = V_c + V_s \quad (7)$$

$$V_c = 0.17\sqrt{f_c'} \cdot b_w \cdot d \quad (8)$$

$$V_s = (2A_s \cdot f_y \cdot b_w)/s \quad (9)$$

where A_s is the area of hoop reinforcement, f_y is the yield strength of the reinforcement steel assumed to be 420 MPa , d is the effective depth typically taken as 0.85 times the lining thickness, $V_c$represents shear capacity provided by the concrete, f_c' is Compressive strength of concrete 30 MPa, b_w is width of the section consider 1m, V_s is shear capacity provided by the hoop reinforcement, and s is spacing of hoop reinforcement. The longitudinal reinforcement is taken as 0.002 times the gross area of the concrete section to satisfy minimum reinforcement requirements.

Table 8 presents the proposed tunnel lining sections along with their corresponding moment and shear capacities. It demonstrates that increasing both the lining thickness and the steel reinforcement from 300 mm in Case 1 to 400 mm in Case 8 enhances structural performance. The calculated moment capacities range from 107.61 kNm/m to 703.07 kNm/m, while shear capacities range from 1081.47 kN/m to 4452.34 kN/m. These values were sufficient to resist the peak internal forces identified in the numerical parametric study as shown in Figures 19-a and 19-b.

Table 8. Tunnel lining sections capacity

Cases	Thickness (mm)	Total concrete Quantity (m^3/m^2)	Hoop reinforcement	Longitudinal reinforcement	Total Reinforcement Weight (Upper & Lower Layers) (kg/ m^2)	Maximum moment M_n (KNm)/m	Maximum shear force V_n (kN)/m
Case 1	300	0.3	φ 16 @ 200	φ 12 @ 150	27.60	107.61	1081.47
Case 2	300	0.3	φ 18 @ 125	φ 12 @ 150	43.77	217.91	1946.60
Case 3	300	0.3	φ 20 @ 125	φ 12 @ 150	51.27	269.03	2347.51
Case 4	300	0.3	φ 20 @ 100	φ 12 @ 150	61.13	336.29	2875.03
Case 5	350	0.35	φ 22 @ 125	φ 12 @ 150	59.55	379.78	2830.20
Case 6	350	0.35	φ 22 @ 100	φ 12 @ 150	71.48	474.73	3468.50
Case 7	350	0.35	φ 28 @ 125	φ 12 @ 150	89.13	615.19	4412.76
Case 8	400	0.4	φ 28 @ 125	φ 12 @ 150	89.13	703.07	4452.34

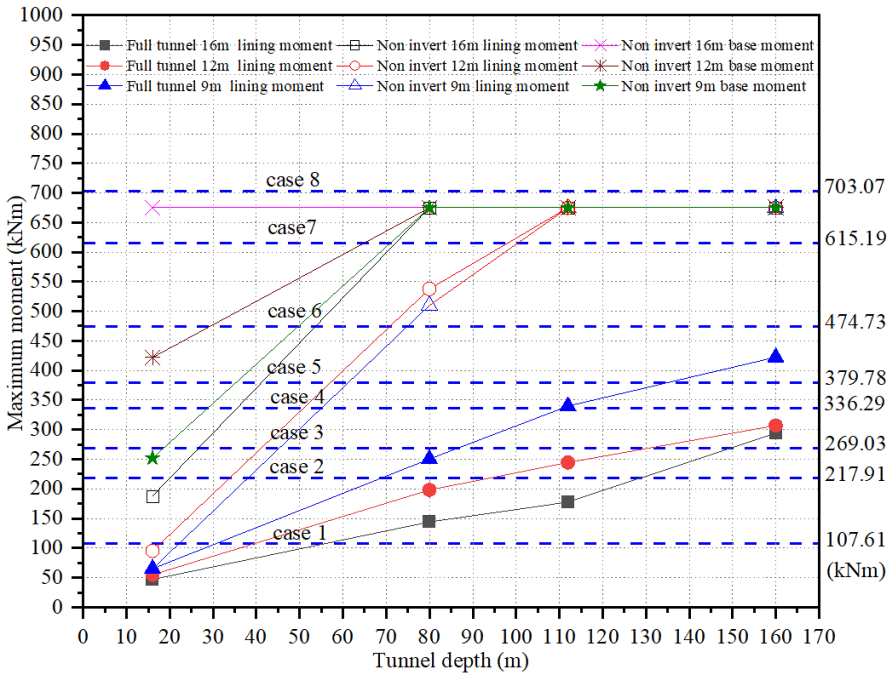

(a) Maximum moment capacity and peak moment values (Cases 1–8)

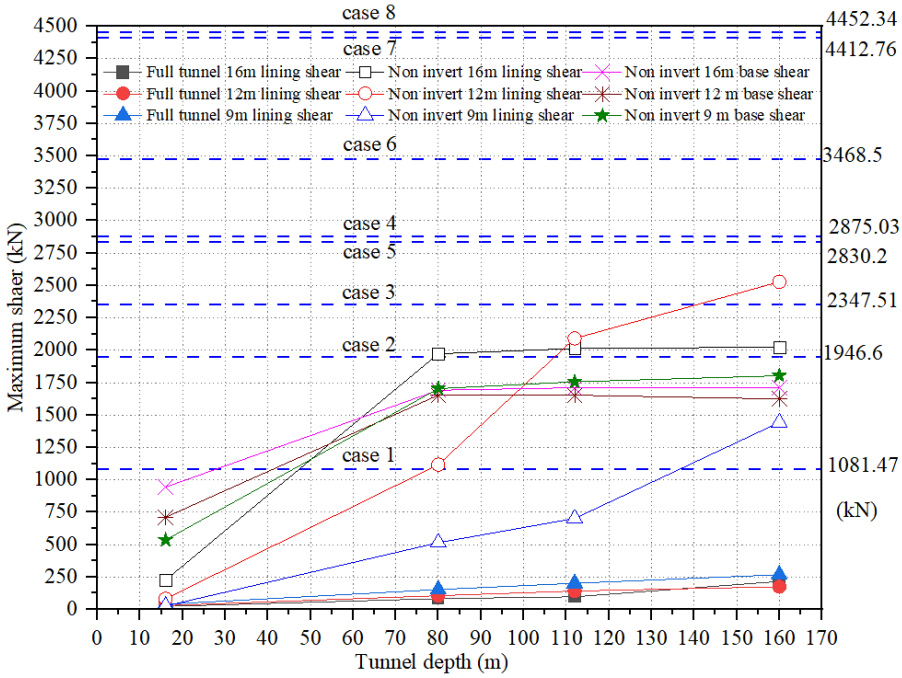

(b) Maximum shear capacity and peak shear values (Cases 1–8)

Figure 19. Maximum moment and shear capacity of tunnel lining sections (Cases 1–8) compared to peak internal forces

Following this evaluation, the next step involves selecting the appropriate lining thickness and reinforcement layout for both circular and non-invert configurations across all tunnel diameters and depths. This selection ensures that each design satisfies structural requirements. Based on the internal forces obtained from the numerical analysis, the most suitable lining section is assigned to each tunnel scenario. Once selected, the corresponding material quantities of concrete and steel are calculated. For the non-invert tunnels, the tunnel base and lining are selected separately. The estimated material demands for each case are summarized in Table 9 and comparative material quantities between non-invert and circular tunnels are illustrated in Figures 20-a and 20-b.

An important consideration when comparing tunnel types is the excavation area as it directly influences construction cost and material demand. Although non-invert tunnels usually have a smaller cross-sectional area than circular tunnels, the need to include roadways, pipelines, drainage, and other utilities often leads to a larger excavation size in practice. As a result, the actual excavation area of non-invert tunnels can become nearly equivalent to that of full circular tunnels. Examples of such configurations are illustrated in Asakura & Kojima [8] and in Xu et al. [2], where the later addition of an invert converted the section into a near circular profile.

Table 9. Tunnel lining concrete and reinforcement steel quantities

Tunnel Type	Tunnel Lining Case/Length (m)	Tunnel Base Case/Length (m)	Lining Concrete (m^3)	Base Concrete (2 Bases) (m^3)	Lining Steel (kg)	Base Steel (2 Bases) (kg)	Total Concrete Qty (m^3/m)	Total Steel Qty (kg/m)
Non-invert D9m at 16 m	Case1/18.85	Case3/1.5	5.66	0.9	520.39	153.81	6.56	674.20
Full tunnel D9m at 16 m	Case1/28.26	-	8.48	0	780.17	0	8.48	780.17
Non-invert D9m at 80 m	Case7/18.85	Case8/1.5	6.60	1.2	1680.12	267.39	7.80	1947.51
Full tunnel D9m at 80 m	Case3/28.26	-	8.48	0	1448.89	0	8.48	1448.89
Non-invert D9m at 112 m	Case8/18.85	Case8/1.5	7.54	1.2	1680.12	267.39	8.74	1947.51
Full tunnel D9m at 112 m	Case5/28.26	-	9.89	0	1682.94	0	9.89	1682.94
Non-invert D9m at 160 m	Case8/18.85	Case8/1.5	7.54	1.2	1680.12	267.39	8.74	1947.51
Full tunnel D9m at 160 m	Case6/28.26	-	9.89	0	2020.08	0	9.89	2020.08
Non-invert D12m at 16m	Case1/25.13	Case6/2.0	7.54	1.4	693.76	285.93	8.94	979.69
Full tunnel D12m at 16m	Case 1/37.68	-	11.30	0	1040.23	0	11.30	1040.23
Non-invert D12m at 80m	Case7/25.13	Case8/2.0	8.80	1.6	2239.86	356.52	10.40	2596.38
Full tunnel D12m at 80 m	Case 2/37.68	-	11.30	0	1649.50	0	11.30	1649.50
Non-invert D12m at 112m	Case8/25.13	Case8/2.0	10.05	1.6	2239.86	356.52	11.65	2596.38
Full tunnel D12m at 112m	Case3/37.68	-	11.30	0	1931.85	0	11.30	1931.85
Non-invert D12m at 160m	Case8/25.13	Case8/2.0	10.05	1.6	2239.86	356.52	11.65	2596.38
Full tunnel D12m at 160m	Case4/37.68	-	11.30	0	2303.36	0	11.30	2303.36
Non-invert D16m at 16 m	Case 2/33.51	Case8/2.5	10.05	2.136	1466.95	475.96	12.19	1942.91
Full tunnel D16m at 16 m	Case 1/50.24	-	15.07	0	1386.97	0	15.07	1386.97
Non-invert D16m at 80 m	Case 8/33.51	Case8/2.5	13.40	2.136	2986.77	475.96	15.54	3462.73
Full tunnel D16m at 80 m	Case 2/50.24	-	15.07	0	2199.34	0	15.07	2199.34
Non-invert D16m at 112m	Case 8/33.51	Case8/2.5	13.40	2.136	2986.77	475.96	15.54	3462.73
Full tunnel D16m at 112m	Case2/50.24	-	15.07	0	2199.34	0	15.07	2199.34
Non-invert D16m at 160m	Case8/33.51	Case8/2.5	13.40	2.136	2986.77	475.96	15.54	3462.73
Full tunnel D16m at 160m	Case4/50.24	-	15.07	0	3071.15	0	15.07	3071.15

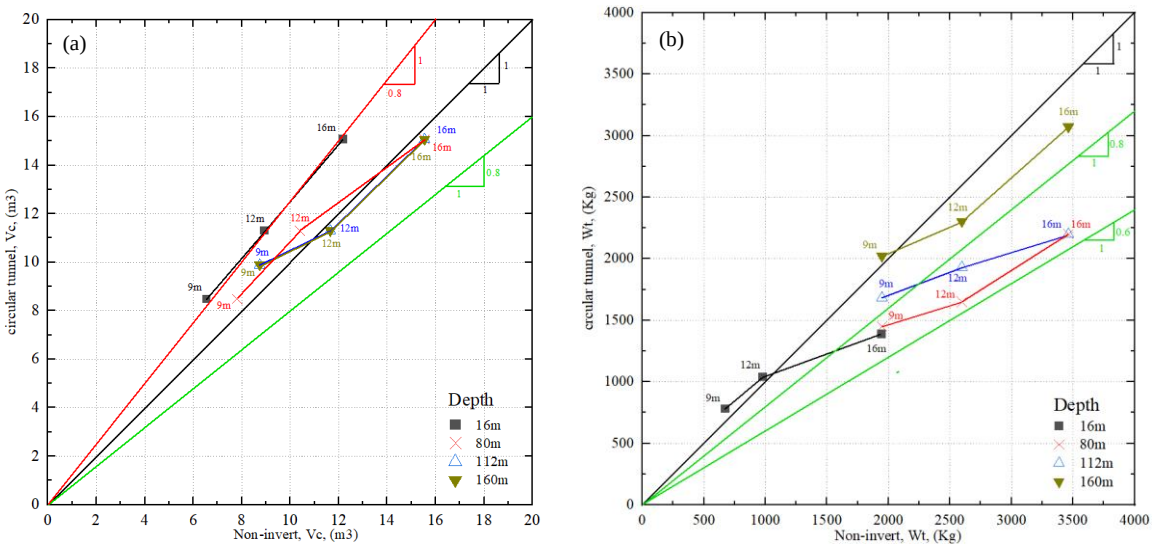

Figure 20. Comparative concrete and reinforcement steel quantities for non-invert and circular tunnels

6. Conclusions

This study systematically evaluates the structural performance and cost efficiency of full circular tunnels versus non-invert tunnels using centrifuge model testing and numerical parametric analysis. The key findings are summarized as follows:

- Full circular tunnel sections demonstrate a more uniform distribution of stresses in both the tunnel lining and the surrounding soil. This results in significantly lower bending moments and shear forces in the tunnel lining compared to non-invert tunnel sections. Additionally, non-invert tunnels exhibit concentrated shear stress in the surrounding soil, particularly near the lower fulcrum corners and springline. Furthermore, non-invert tunnels show more pronounced settlement at the upper surface and heaving at the invert compared to circular tunnels.
- At a depth of 16 m, the non-invert configuration is more economical for 9 m and 12 m diameters, reducing steel consumption by 6–14% and concrete use by 21–23%. However, for a 16 m diameter, the circular tunnel was more cost-effective, lowering steel demand by 29% despite a 19% increase in concrete. Given that concrete accounts for only 10–15% of the cost of steel, the steel savings outweighed the additional concrete cost.
- At a depth of 80m, circular tunnels are more economical across all diameters, providing a 26–36% reduction in steel usage. For 16 m diameter, the circular tunnel design also reduces concrete use by around 3%. Although circular tunnels require about 8% more concrete than non-invert tunnels at a 9 m and 12 m diameters, the associated steel savings still made the circular tunnels configuration the most cost-effective option.
- At a depth of 112 m, circular tunnels are more economical across all diameters, providing a 14–36% reduction in steel usage. For 12 m and 16 m diameters, the circular tunnels design also reduce concrete use by around 3%. Although circular tunnels require about 8% more concrete than non-invert tunnel at a 9 m diameter, the steel savings still result in a more cost-effective solution.
- At a depth of 160 m, the non-invert tunnel is more economical only at a 9 m diameter, with 4% less steel and 12% less concrete required. For 12 m and 16 m diameters, the circular tunnels remain the most cost-effective choice, reducing steel use by 11% and concrete by 3%.

Overall, the interaction between tunnel depth and diameter is a key factor in design optimization. While non-invert tunnels offer modest material savings at shallow depths and smaller diameters with reductions of up to 14% in steel and 23% in concrete. However, these initial savings are often insufficient to offset future maintenance costs. Such costs may include the installation of new reinforced concrete inverts or even new tunnel construction as demonstrated in the Tenjin Yama Tunnel [1]. Circular tunnels, while requiring up to 19% more concrete, achieve up to 36% steel savings and provide more uniform stress distribution. Since concrete costs only 10–15% of steel, circular tunnels are generally more economical at greater depths and larger diameters.

6.1. Limitation

This study focuses on material-based cost comparisons, including concrete and steel reinforcement quantities. However, construction practicality, such as ease of excavation, formwork complexity, labor intensity, and installation time are not explicitly considered. These factors can significantly affect real-world feasibility and should be addressed in future research to support a more comprehensive economic assessment of tunnel design alternatives.

7. Declarations

7.1. Author Contributions

Conceptualization, A.D. and K.U.; methodology, A.D. and K.U.; software, A.D.; validation, A.D. and K.U. formal analysis, A.D. and K.U.; investigation, A.D. and K.U.; resources, K.U.; data curation, A.D.; writing—original draft preparation, A.D.; writing—review and editing, A.D. and K.U.; visualization, A.D. and K.U.; supervision, K.U.; project administration, K.U.; funding acquisition, K.U. All authors have read and agreed to the published version of the manuscript.

7.2. Data Availability Statement

The data presented in this study are available on request from the corresponding author.

7.3. Funding and Acknowledgment

This research was supported by Tokushima University; under the Disaster Prevention Science Geotechnical Engineering Lab. The authors gratefully acknowledge the funding provided for conducting centrifuge model tests.

7.4. Conflicts of Interest

The authors declare no conflict of interest.

8. References

[1] Komatani, D., Yokoo, K., & Akagi, W. (2018). Effect of rock bolt construction under tunnel roadbed on suppressing road surface upheaval. Proceedings of Annual Conference of the Japan Society of Civil Engineers, VI-062, 123-124.

[2] Xu, S., Ma, E., Lai, J., Yang, Y., Liu, H., Yang, C., & Hu, Q. (2022). Diseases failures characteristics and countermeasures of expressway tunnel of water-rich strata: A case study. Engineering Failure Analysis, 134, 106056. doi:10.1016/j.engfailanal.2022.106056.

[3] Du, M., Wang, X., Zhang, Y., Li, L., & Zhang, P. (2020). In-situ monitoring and analysis of tunnel floor heave process. Engineering Failure Analysis, 109, 104323. doi:10.1016/j.engfailanal.2019.104323.

[4] Zan, W., Liu, L., Lai, J., Wang, E., Zhou, Y., & Yang, Q. (2023). Deformation failure characteristics of weathered phyllite tunnel and variable-stiffness support countermeasures: A case study. Engineering Failure Analysis, 153, 107553. doi:10.1016/j.engfailanal.2023.107553.

[5] Isago, N., Kawata, K., Kusaka, A., & Ishimura, T. (2015). Long-term deformation of mountain tunnel lining and ground under swelling rock condition. Geomechanik Und Tunnelbau, 8(5), 380–386. doi:10.1002/geot.201500024.

[6] Li, C., & Wu, Y. (2025). Analysis and control of the causes of the uplift of the invert of deep tunnels. Discover Applied Sciences, 7(1), 11. doi:10.1007/s42452-024-06424-w.

[7] Fan, R., Chen, T., Yin, X., Wang, G., Li, M., & Wang, S. (2024). Analysis of Mechanical Properties of Steep Surrounding Rock and Failure Process with Countermeasures for Tunnel Bottom Structures. Applied Sciences (Switzerland), 14(18), 8341. doi:10.3390/app14188341.

[8] Asakura, T., & Kojima, Y. (2003). Tunnel maintenance in Japan. Tunnelling and Underground Space Technology, 18(2–3), 161–169. doi:10.1016/S0886-7798(03)00024-5.

[9] Huang, C., Li, S., Li, G., Yao, T., & Wu, X. (2024). Reform of deformation control technology for railway tunnels with squeezing surrounding rock: case study of the new and existing Wushaoling tunnels in China. Frontiers in Earth Science, 12. doi:10.3389/feart.2024.1438425.

[10] Li, T. (2012). Damage to mountain tunnels related to the Wenchuan earthquake and some suggestions for aseismic tunnel construction. Bulletin of Engineering Geology and the Environment, 71(2), 297–308. doi:10.1007/s10064-011-0367-6.

[11] Yashiro, K., Shimamoto, K., & Kojima, Y. (2011). Guidelines for Selection of Appropriate Seismic Countermeasures for Existing Mountain Tunnels in Poor Geological Conditions. Quarterly Report of RTRI, 52(4), 210–216. doi:10.2219/rtriqr.52.210.

[12] Lu, C.-C., & Hwang, J.-H. (2008). Damage of New Sanyi Railway Tunnel during the 1999 Chi-Chi Earthquake. In Geotechnical Earthquake Engineering and Soil Dynamics IV, 1–10. doi:10.1061/40975(318)207.

[13] Mothersille, D., & Littlejohn, S. (2012). Grouting of Anchors to Resist Hydrostatic Uplift at Burnley Tunnel, Melbourne, Australia. Grouting and Deep Mixing, 1073–1084. doi:10.1061/9780784412350.0088.

[14] Zheng, X., Huang, F., Wang, S., & Xu, W. (2024). Research on the Mechanism of Loose Deformation in Weak Fracture Zone Tunnel Surrounding Rock and Support Control. Buildings, 14(8), 2506. doi:10.3390/buildings14082506.

[15] Saraswat, S., & Maheshwari, B. K. (2024). Seismic Behaviour of Tunnels of Different Shapes in Rocks. Japanese Geotechnical Society Special Publication, 10(20), 730–735. doi:10.3208/jgssp.v10.os-9-05.

[16] Ng, C. W. W., Wang, R., & Boonyarak, T. (2016). A comparative study of the different responses of circular and horseshoe-shaped tunnels to an advancing tunnel underneath. Geotechnique Letters, 6(2), 168–175. doi:10.1680/jgele.16.00001.

[17] Ma, K., Li, W., Li, J., Wang, H., Zheng, J., & Zhang, J. (2020). Research on the Mechanism and Treatment Technique of Invert Floor Heave after the Penetration of Large Cross-section Tunnel in Slight Inclined Stratum. IOP Conference Series: Earth and Environmental Science, 570(5), 52031. doi:10.1088/1755-1315/570/5/052031.

[18] Dang, V. K., Do, N. A., & Dinh, V. D. (2022). Estimating the Radial Displacement on the Tunnel Boundary by Rock Mass Classification Systems. International Journal of GEOMATE, 22(92), 9–15. doi:10.21660/2022.92.19.

[19] Lopez Ochoa, J. (2024). Modelling long-term deterioration of lining in tunnels. Ph.D. Thesis, Politecnico di Torino, Turin, Italy.

[20] Farhadian, H., & Gholami, Z. (2024). Hydraulic Response to Geometry: Finite Element Modeling of Underground Spaces in Saturated Environments. Journal of Hydraulic Structures, 10(1), 66–79.

[21] Han, Z., Liu, K., Ma, J., & Li, D. (2024). Numerical simulation on the dynamic mechanical response and fracture mechanism of rocks containing a single hole. International Journal of Coal Science and Technology, 11(1), 64. doi:10.1007/s40789-024-00718-5.

[22] Nie, F., Zhang, X., Zhou, L., Wang, H., Hua, J., Liu, B., & Feng, B. (2025). Investigation of Fracture Characteristics and Energy Evolution Laws of Model Tunnels with Different Shapes Subjected to Impact Load. Materials, 18(4), 889. doi:10.3390/ma18040889.

[23] Ma, X., Tang, G., Ma, C., & Zhang, H. (2025). Seismic response of cross-passages between parallel tunnels with varied connection rigidities in centrifuge model tests. Soil Dynamics and Earthquake Engineering, 194, 109385. doi:10.1016/j.soildyn.2025.109385.

[24] Weng, X., Dang, B., Li, X., Ye, F., & Ma, Y. (2025). Study on the instability mode of a tunnel face under variable seepage conditions in sandy soil shield tunnels: Centrifuge tests and numerical simulation. Tunnelling and Underground Space Technology, 159, 106515. doi:10.1016/j.tust.2025.106515.

[25] Zhang, J., Wang, A., & Chen, X. (2025). Deformation and strain mechanisms of an existing tunnel subject to failure of a new tunnel. International Journal of Geotechnical Engineering, 19(4), 147–57. doi:10.1080/19386362.2025.2471771.

[26] Shibayama, S., Izawa, J., Takahashi, A., Takemura, J., & Kusakabe, O. (2010). Observed behaviour of a tunnel in sand subjected to shear deformation in a centrifuge. Soils and Foundations, 50(2), 281–294. doi:10.3208/sandf.50.281.

[27] Behnen, G., Nevrly, T., & Fischer, O. (2015). Soil-structure interaction in tunnel lining analyses. Geotechnik, 38(2), 96–106. doi:10.1002/gete.201400010.

[28] Ueno, K. (1998). Methods for preparation of sand samples. Proceedings of the International Conference Centrifuge, 23-25 September, 1998, Tokyo, Japan.

[29] OPTUM G2 (2023). Optum G2 – 2D Geotechnical Design & analysis Software. Optum Computational Engineering, Newcastle, New South Wales, Australia. Available online: www.optumce.com (accessed on May 2025).

[30] Eslon Plant. (2025). UPVC Pipes. Eslon Plant, Osaka, Japan. Available online: www.eslon-plant.jp (accessed on May 2025). (In Japanese).

[31] Cai, M., Kaiser, P. K., Tasaka, Y., Maejima, T., Morioka, H., & Minami, M. (2004). Generalized crack initiation and crack damage stress thresholds of brittle rock masses near underground excavations. International Journal of Rock Mechanics and Mining Sciences, 41(5), 833–847. doi:10.1016/j.ijrmms.2004.02.001.

[32] Wu, H., Zhao, G., & Ma, S. (2022). Failure behavior of horseshoe-shaped tunnel in hard rock under high stress: Phenomenon and mechanisms. Transactions of Nonferrous Metals Society of China, 32(2), 639–656. doi:10.1016/s1003-6326(22)65822-9.

[33] Liu, S., Shi, Y., Sun, R., & Yang, J. (2020). Damage behavior and maintenance design of tunnel lining based on numerical evaluation. Engineering Failure Analysis, 109, 104209. doi:10.1016/j.engfailanal.2019.104209.

[34] Penzien, J., & Wu, C. L. (1998). Stresses in linings of bored tunnels. Earthquake Engineering and Structural Dynamics, 27(3), 283–300. doi:10.1002/(SICI)1096-9845(199803)27:3<283::AID-EQE732>3.0.CO;2-T.

[35] Zeng, X. T., Wang, S. J., & Lv, Z. T. (2024). Stress solution for an arbitrarily shaped tunnel with a neighboring circular cavity. Mathematics and Mechanics of Solids, 29(1), 83–98. doi:10.1177/10812865231187853.

[36] Luo, Y., Chen, J., Chen, Y., Diao, P., & Qiao, X. (2018). Longitudinal deformation profile of a tunnel in weak rock mass by using the back analysis method. Tunnelling and Underground Space Technology, 71, 478–493. doi:10.1016/j.tust.2017.10.003.

[37] Hoek, E. (1998). Tunnel support in weak rock. Keynote address, symposium of sedimentary rock engineering, 20-22 November, 1998, Taipei, Taiwan.

[38] Tang, S. B., & Tang, C. A. (2012). Numerical studies on tunnel floor heave in swelling ground under humid conditions. International Journal of Rock Mechanics and Mining Sciences, 55, 139–150. doi:10.1016/j.ijrmms.2012.07.007.

[39] Gokceoglu, C., Aygar, E. B., Nefeslioglu, H. A., Karahan, S., & Gullu, S. (2022). A Geotechnical Perspective on a Complex Geological Environment in a High-Speed Railway Tunnel Excavation (A Case Study from Türkiye). Infrastructures, 7(11), 155. doi:10.3390/infrastructures7110155.

[40] Barla, M. (1999). Tunnels in swelling ground: simulation of 3D stress paths by triaxial laboratory testing. Ph.D. Thesis, Università degli Studi di Genova, Genoa, Italy.

[41] Cao, C., Shi, C., Lei, M., Peng, L., & Bai, R. (2018). Deformation Characteristics and Countermeasures of shallow and Large-span Tunnel Under-crossing the Existing Highway in Soft Soil: a Case Study. KSCE Journal of Civil Engineering, 22(8), 3170–3181. doi:10.1007/s12205-017-1586-6.

[42] ACI 318-19. (2019). Building Code Requirements for Structural Concrete (ACI 318-19) and Commentary (ACI 318R-19). American Concrete Institute (ACI), Farmington Hills, United States.